

Cite this: *J. Mater. Chem. A*, 2024, 12, 13191

Self-adhesive polyelectrolyte hydrogel electrolytes for long-life flexible zinc-ion batteries†

Yahui Xu,^{ab} Binxu Lan,^b Yin Cheng,^b Liangjing Shi,^b Jing Sun,^b Shijiao Sun^{*a} and Ranran Wang^{†bc}

Hydrogel electrolytes have a wide range of promising applications in flexible zinc-ion batteries (ZIBs) due to their high ionic conductivity and soft wetting properties. However, poor electrode/electrolyte interfacial compatibility leads to sluggish ion transport and interfacial side reactions that reduce the cycle life of the cell. Herein, a zwitterionic sulfobetaine/acrylamide hydrogel electrolyte with self-adhesive and stable electrochemical properties was investigated to address the above problems. This hydrogel electrolyte possesses excellent tensile properties (620%), self-adhesive properties, ionic conductivity (59.0 mS cm⁻¹) and Zn²⁺ transference number (0.81). Meanwhile, the special zwitterionic structure can construct separated anion and cation migration channels to promote ion transport and uniform deposition of Zn²⁺. The ZIBs assembled with the zwitterionic hydrogel electrolyte exhibit excellent electrochemical performance with a high specific discharge capacity of 292 mA h g⁻¹ at 5 A g⁻¹ and a capacity retention of 94.7% after 1000 cycles. In addition, flexible pouch ZIBs based on zwitterionic hydrogel electrolytes were designed, which can work properly when subjected to different types of damage and offer great potential in the field of flexible wearable energy storage.

Received 19th February 2024

Accepted 25th April 2024

DOI: 10.1039/d4ta01125b

rsc.li/materials-a

1. Introduction

In recent years, the growing crises of energy shortage and serious environmental damage have facilitated the exploration and development of sustainable energy storage technologies.^{1–3} Meanwhile, with the booming development of flexible wearable electronic devices, higher requirements for energy storage devices have been put forward.^{4–6} ZIBs have gained much attention due to their low redox potential (−0.763 V vs. SHE), high theoretical capacity (820 mA h g⁻¹), low cost, and high safety.^{7–9} As an important part of ZIBs, the electrolyte plays a key role in promoting ion transport and increasing the battery's cycle life.¹⁰ For energy storage devices composed of liquid electrolytes (LEs), mechanical damage is inevitable during daily use, resulting in safety issues such as explosion and corrosion caused by leakage.⁷ What's more, a large amount of highly reactive free H₂O and Zn²⁺ interact in a liquid environment to

form a solvation layer, leading to the uncontrollable growth of zinc dendrites and side reactions, which greatly reduce the battery's cycle life.^{11,12} For solid-state electrolytes, the lower ionic conductivity and poor interfacial compatibility are also not suitable for the flexible wearable field.¹³ In contrast, soft and wet hydrogel electrolytes with high ionic conductivity similar to that of liquid electrolytes and mechanical flexibility superior to that of solid-state electrolytes have received a lot of attention and are better used in the field of wearable energy storage devices.^{14,15}

Previously, many scholars have investigated hydrogel electrolytes based on matrices such as polyacrylamide (PAM),¹⁶ polyvinyl alcohol (PVA),¹⁷ gelatin,¹⁸ polyacrylic acid (PAA),¹⁹ and cellulose.²⁰ For example, Li *et al.* designed a gelatin and PAM-based hydrogel electrolyte to fabricate a flexible zinc-ion battery with excellent flexibility and safety properties, which can maintain normal operation under various destructive or harsh conditions.²¹ Wang *et al.* reported a nanofibrillated cellulose (NFC)/polyacrylamide (PAM) hydrogel that exhibited tensile strains up to 1100%.²² Despite the great advantages of hydrogel electrolytes in terms of flexibility and safety, there are still many critical issues that need to be further optimized and solved. Firstly, an ideal hydrogel electrolyte should have a high ionic conductivity, whereas the conventional gel matrix outlined earlier can only provide a physical framework to support ionic transport and cannot serve to enhance electrochemical performance. According to the current reported studies, zwitterionic polymers are promising electrolyte components and electrode modification materials. Zhuo *et al.* designed a polymer

^aState Key Laboratory of Materials-Oriented Chemical Engineering, College of Materials Science and Engineering, Nanjing Tech University, 30 Puzhu South Road, Nanjing 211816, China. E-mail: sunshijiao@njtech.edu.cn

^bState Key Laboratory of High Performance Ceramics and Superfine Microstructure, Shanghai Institute of Ceramics, Chinese Academy of Sciences, 1295 Ding Xi Road, Shanghai 200050, China. E-mail: wangranran@mail.sic.ac.cn

^cSchool of Chemistry and Materials Science, Hangzhou Institute for Advanced Study, University of Chinese Academy of Sciences, 1 Sub-lane Xiangshan, Hangzhou 310024, China

† Electronic supplementary information (ESI) available. See DOI: <https://doi.org/10.1039/d4ta01125b>

poly(pyrrole-squaraine) base (PPS) cathode material that contained a zwitterionic structure. Precise control of the size of the zwitterionic polymer micro/nanospheres was achieved by changing the preparation conditions, and the size control of the organic material and its effect on sodium storage were investigated.²³ When zwitterionic polymers are used as electrolytes, the unique structure allows strong interactions with the polymer groups and also builds a Zn^{2+} fast migration network through electrostatic interactions with water molecules, which has become a hot research topic.^{24,25} For example, Leng *et al.* reported a zwitterionic hydrogel electrolyte exhibiting high ionic conductivity (32 mS cm^{-1}) and Zn^{2+} transference number (0.66) as well as excellent battery cycle life.²⁶ Secondly, the main reaction of ZIBs occurs at the electrode/electrolyte interface, and it is important to maintain low interfacial impedance and electrochemical stability. In addition, during the use of flexible zinc-ion batteries, it is inevitable that they will be damaged by external mechanical forces, leading to a decrease in battery performance or even failure.²⁷ Therefore, higher requirements are placed on the strength of the interfacial affinity between the electrode material and the gel electrolyte and on the high mechanical strength of the hydrogel electrolyte.

In this study, we introduced zwitterionic sulfobetaine [2-(methacryloyloxy)ethyl]dimethyl-(3-sulfopropyl) (SBMA) and acrylamide (AM) to prepare a polyzwitterionic hydrogel electrolyte (PSAZn-gel) with enhanced mechanical properties, adhesion properties, and ionic migration channels. In particular, PSAZn-gel exhibits a high elongation at break of 620% benefiting from the combined effect of physical and chemical cross-linking networks. Thanks to the synergistic effect of multiple interactions (including hydrogen bonding, electrostatic interactions, metal coordination, *etc.*), the hydrogel electrolyte is endowed with favorable adhesion performance, with an adhesion strength as high as 108 kPa with zinc foil, which is important for maintaining the stability of the flexible device during the deformation process. What's more, the special structural zwitterionic structure of SBMA can establish ionic migration channels to guide and promote the uniform and efficient transport of ions, enabling the battery to exhibit excellent electrochemical performance. The $\text{Zn}||\text{NH}_4\text{V}_4\text{O}_{10}$ cell prepared with PSAZn-gel electrolyte is able to provide a high specific capacity of 292 mA h g^{-1} at a current density of 5 A g^{-1} . And the capacity retention is 94.7% after 1000 cycles. At a current density of 1 mA cm^{-2} with a cut-off capacity of 1 mA h cm^{-2} , the $\text{Zn}||\text{PSAZn-gel}||\text{Zn}$ cell can achieve a stable cycle life of 800 h. Furthermore, a flexible planar structure battery is prepared using PSAZn-gel electrolyte with 96.9% capacity retention after 500 charge/discharge cycles at 5 A g^{-1} . These cells have excellent flexibility and can provide stable performance output even after bending at different angles, offering great potential for flexible wearable applications.

2. Results and discussion

2.1 Preparation and characterization of the hydrogel

As shown in Fig. 1a, the PSAZn-gel electrolyte was prepared by the one-pot method, in which two monomers (AM and SBMA),

$\text{Zn}(\text{TFSI})_2$, a crosslinker (MBAA) and an initiator (KPS) were mixed and added to the vessel and stirred well, and then thermally initiated at $60 \text{ }^\circ\text{C}$. The same method was also used to prepare a PAM hydrogel (hereinafter abbreviated as PAZn-gel) electrolyte as a control. Fourier-transform infrared (FTIR) spectroscopy was used to characterize the chemical structure and polymerization mechanism of the hydrogel (Fig. 1b). The C=O characteristic absorption peak is detected at 1653 cm^{-1} , the N-H stretching vibration peaks are detected at 1605 and 3189 cm^{-1} , and the C-N stretching vibration peaks are detected at 1445 and 1411 cm^{-1} , and they are all from the PAM chain segment. Furthermore, the characteristic absorption peaks at 1176 and 1038 cm^{-1} are from the $-\text{SO}_3^-$ group in SBMA. Importantly, the absence of the characteristic absorption peaks of C=C ($\approx 1635 \text{ cm}^{-1}$) in the FTIR spectrum of PSAZn-gel proves that the two monomer substances have been successfully polymerized through the opening and joining of double bonds.²⁸ Moreover, the special peaks in the range of $1280\text{--}1800 \text{ cm}^{-1}$ were analyzed (Fig. S1†). Compared with PAZn-gel, the C=O and N-H absorption peaks in PSAZn-gel are shifted to higher wave numbers, indicating the enhancement of hydrogen bonding between hydrogels.²⁹ What's more, no obvious characteristic absorption peaks are present at 1303 cm^{-1} due to the effect of electrostatic interactions between the charged groups after polymerization.^{30,31} Based on the synergistic effect of the enhanced hydrogen bonding, crosslinked network and electrostatic interactions, it is possible to reduce the size of the phase-separation region within the PSAZn-gel, which provides an advantageous promotion of the fracture elongation and adhesion of the hydrogel. The scanning electron microscopy (SEM) images demonstrate the three-dimensional (3D) network structure of two hydrogels. PAZn-gel exhibits a non-uniform network structure (Fig. S2†), whereas PSAZn-gel has numerous homogeneous interconnected pores and channel structures (Fig. 1c), which facilitates the free movement of ions inside the gel electrolyte for more efficient electrochemical reactions. The charged groups on the SBMA chains may coordinate with Zn^{2+} and influence their transportation. To investigate the binding sites of Zn^{2+} in PSAZn-gel, electrostatic potential (ESP) distribution calculations were performed. As shown in Fig. 1d, the negative electrons on the SBMA chain are mainly concentrated on the oxygen atom of the $-\text{SO}_3^-$ group, which is a highly active site for interaction with Zn^{2+} and favors the formation of the coordination structure of $\text{Zn}^{2+}\text{--SBMA}$.

In the course of daily use, flexible zinc-ion batteries inevitably undergo shape changes and a certain degree of damage, which leads to an increase in the internal resistance of batteries and triggers the acceleration of interfacial side reactions.³² This requires that the hydrogel electrolytes have excellent mechanical properties, which can adapt to deformation by external forces without being damaged. The mechanical properties of hydrogel electrolytes were tested by tensile testing, and the results show that the PSAZn-gel electrolyte has an elongation at break of up to 620% and a fracture strength of 21.1 kPa (Fig. 1e). Likewise, the tensile recovery properties of the PSAZn-gel electrolyte were tested (Fig. 1f). Five consecutive loading-unloading cycles were performed at a maximum tensile strain of 100%,

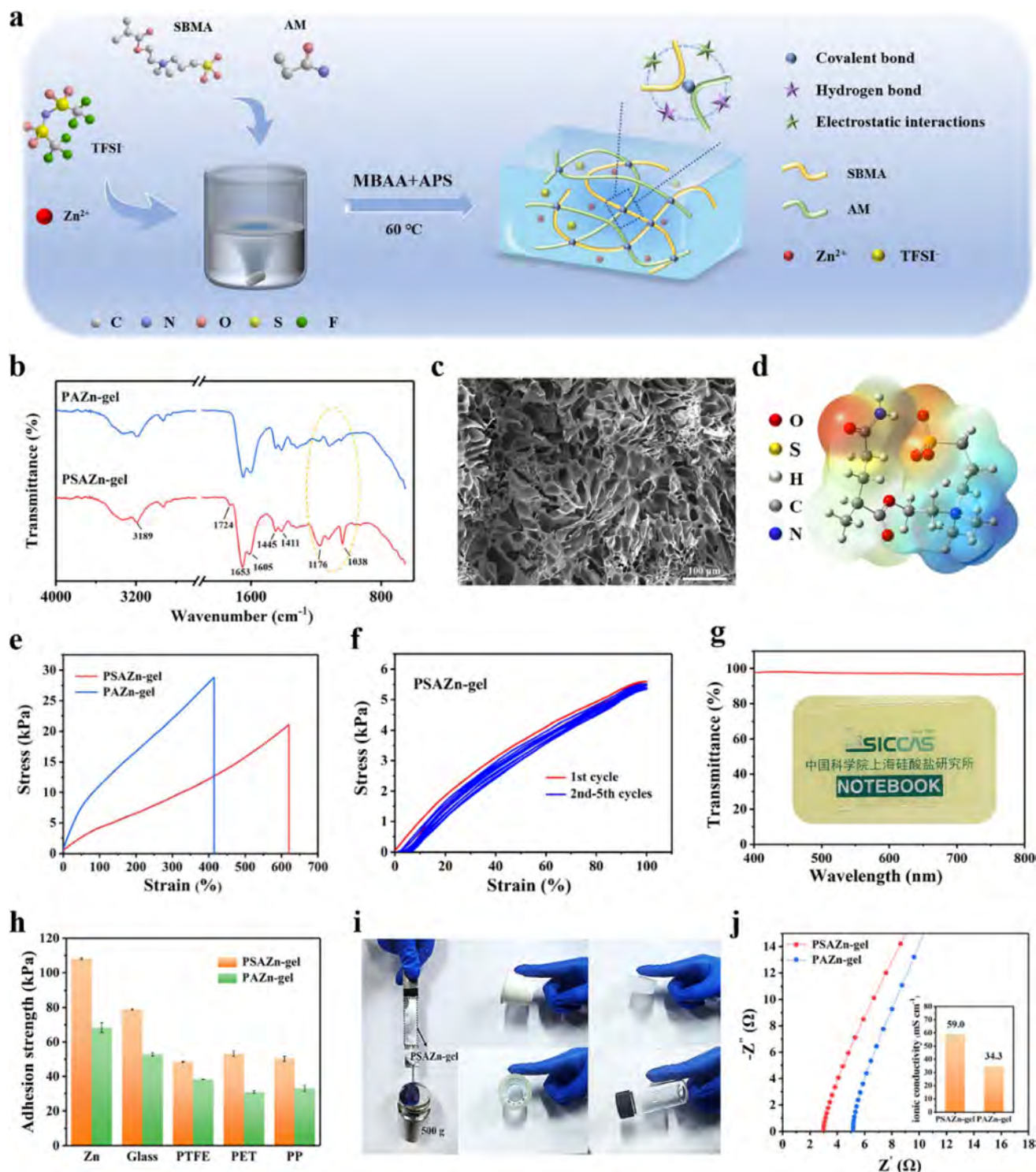


Fig. 1 Preparation and characterization of hydrogel properties. (a) Preparation of PSAZn-gel electrolyte and the schematic diagram of various interactions within the gel. (b) FTIR spectra of PSAZn-gel and PAZn-gel. (c) Cross-section SEM image of PSAZn-gel. (d) Electrostatic potential distribution (ESP) of PSAZn-gel. (e) Tensile stress–strain curves of PSAZn-gel and PAZn-gel. (f) Cyclic loading–unloading curves of PSAZn-gel at 100% strain. (g) UV-vis transmission curve of PSAZn-gel. (h) Adhesion strength of PSAZn-gel and PAZn-gel with different materials. (i) Schematic of the NHVO@Ti/PSAZn-gel/Zn sandwich structure loaded with 500 g weights and interfacial adhesion between PSAZn-gel and paper cups, plastics, tapes and glass. (j) Ionic conductivity of PSAZn-gel and PAZn-gel electrolytes.

and the curves under different cycles almost overlapped with only 7.5% residual strains. On one hand, the excellent mechanical properties of PSAZn-gel are attributed to the

covalently cross-linked network, which allows the hydrogel to maintain the stability of the network conformation when subjected to stress. On the other hand, it benefits from hydrogen

bonding as a reversible sacrificial bond, dissipating energy by breaking and recombining.³³ The transparency of the hydrogel electrolyte is also valuable for the symmetrical arrangement of the electrodes during the assembly of the battery. The UV-vis spectrum (Fig. 1g) shows that the PSAZn-gel hydrogel has a high transmittance of 97% in the visible wavelength range of 400–800 nm, and the photo in the inset shows the high transparency of PSAZn-gel more visually.

During the use of flexible devices, electrolytes with high adhesion strength can better maintain a stable combination between the electrode and electrolyte. The adhesion strength between hydrogels and different substrates (zinc foil, glass, polytetrafluoroethylene (PTFE), PET, and PP) was tested (Fig. 1h). The specific test method is shown in Fig. S3.† The hydrogel on the indenter was placed in contact with the substrate, and then a pre-pressure of 20 N was applied for 90 s. Then the gel was lifted at a speed of 200 mm min⁻¹, causing the peeling off of the gel from the substrate, and the adhesion strength between the gel and the different materials was calculated. It is obvious from the comparative analysis that the adhesion between PSAZn-gel and different substrates is clearly higher than that of PAZn-gel, most notably with zinc foil, and can reach an adhesion strength of 108 kPa. This is partly explained by the fact that the charged groups and reinforced hydrogen bonds increase the inner cohesive force of the gels. Furthermore, metal coordination and electrostatic interactions between the zwitterionic polymer and Zn metal provide an even more favorable adhesion enhancement. As demonstrated by Fig. 1i, the ammonium vanadate (NH₄V₄O₁₀, NHVO)/PSAZn-gel/Zn sandwich structure has excellent adhesion properties and is able to withstand a weight of 500 g without falling off. Moreover, the PSAZn-gel electrolyte has generalized high adhesion to a variety of substrates such as paper cups, adhesive tape, plastics, and glass. Based on the above experimental results, it is found that the addition of PSAZn-gel electrolyte with zwitterionic ions can reduce the elastic modulus of the hydrogel and enhance its own adhesion properties. This change makes the hydrogel electrolyte have a softer and more stable state, which can adapt excellently to the shape change of the electrode surface when in contact with the electrode, thus ensuring better interfacial compatibility and stability.

What's more, the ionic conductivity (σ) of the hydrogel was tested by electrochemical impedance spectroscopy (EIS) (Fig. 1j) and calculated using eqn (1):³⁴

$$\sigma = \frac{L}{RA} \times 10^3 \quad (1)$$

where L and A are the thickness and area of the hydrogel, respectively, and R is the resistance.

The ionic conductivity of the PSAZn-gel electrolyte is 59.0 mS cm⁻¹ at room temperature, which is much better than that of the PAZn-gel electrolyte (34.3 mS cm⁻¹). This is attributed to the more uniform porous network structure of the PSAZn-gel electrolyte, which promotes uniform and rapid ionic transport. Besides, the remarkable ion dissociation ability³⁵ of SBMA and the presence of ion transport channels inside the hydrogel also contribute greatly to the ionic conductivity enhancement. As

shown in Table S1,† the excellent overall stability of PSAZn-gel is demonstrated by comparing elongation, adhesion strength, ionic conductivity, and Zn²⁺ transference number of PSAZn-gel in this work with those in previously reported work.

2.2 Electrochemical performance of hydrogel electrolyte ZIBs

To characterize the electrochemical performance of hydrogel electrolytes, Zn||NHVO cells were assembled, and the detailed preparation process, structural characterization, and battery assembly of NHVO cathode materials are shown in Fig. S4, S5, S6 and S7,† respectively. Electrochemical impedance spectroscopy (EIS) was performed on Zn||NHVO cells in the frequency range of 0.01 Hz to 100 kHz at 1.36 V potential. The intersection of the curve with the real part is the contact resistance (R_c) in the high-frequency region, contributed by both the electrode and the electrolyte, and the linear region is corresponding to the Warburg diffusion process.³⁶ It is obvious from the Nyquist plot (Fig. 2a) that the charge transfer resistance (R_{ct}) of the PSAZn-gel electrolyte is significantly smaller than that of the PAZn-gel electrolyte. It is also easy to see from the inset that in the high-frequency region, the contact resistance of the PSAZn-gel electrolyte is also lower than that of the PAZn-gel electrolyte. In the low-frequency region (Fig. S8†), the slope of the PSAZn-gel electrolyte is significantly smaller, indicating that the ions have excellent diffusion and transport at the interface between the electrolyte and the electrode. The above results demonstrate that the incorporation of zwitterionic ions in the PSAZn-gel electrolyte effectively promotes the compatibility of the electrolyte with the electrode and facilitates the rapid movement of Zn²⁺.

In ZIBs, a high Zn²⁺ ion transference number ($t_{Zn^{2+}}$) plays a key role in the uniform distribution of ions at the anode interface, the reduction of the concentration polarization, and the achievement of high-energy density of cells.^{37,38} As shown in Fig. 2b, $t_{Zn^{2+}}$ of Zn||PSAZn-gel||Zn symmetric cells was tested by the steady current method ($i-t$) at a constant polarization potential of 10 mV. According to the following eqn (2):

$$t_{Zn^{2+}} = \frac{I_s(\Delta V - I_0 R_0)}{I_0(\Delta V - I_s R_s)} \quad (2)$$

where I_0 is the initial current, I_s is the steady-state current, ΔV is the applied polarization voltage, R_0 is the initial resistance, and R_s is the steady-state resistance. The Zn²⁺ transference number of the PSAZn-gel electrolyte was calculated to be as high as 0.81, indicating that it has faster Zn²⁺ transport dynamics. According to Sand's time, higher $t_{Zn^{2+}}$ means that it takes longer for dendrites to be produced during electrochemical deposition.³⁹ This excellent performance is mainly due to the following reasons: (1) the charged groups on the zwitterionic polymer chains promote the dissociation of Zn(TFSI)₂, which establishes specific ion migration channels and accelerates the migration of Zn²⁺.^{40,41} (2) Due to the electrostatic effect and spatial site resistance of the hydrogel network, the movement of the larger anion TFSI⁻ can be hindered to a certain extent.²⁶ (3) Under the effect of electrostatic interactions, the amphiphilic ionic groups

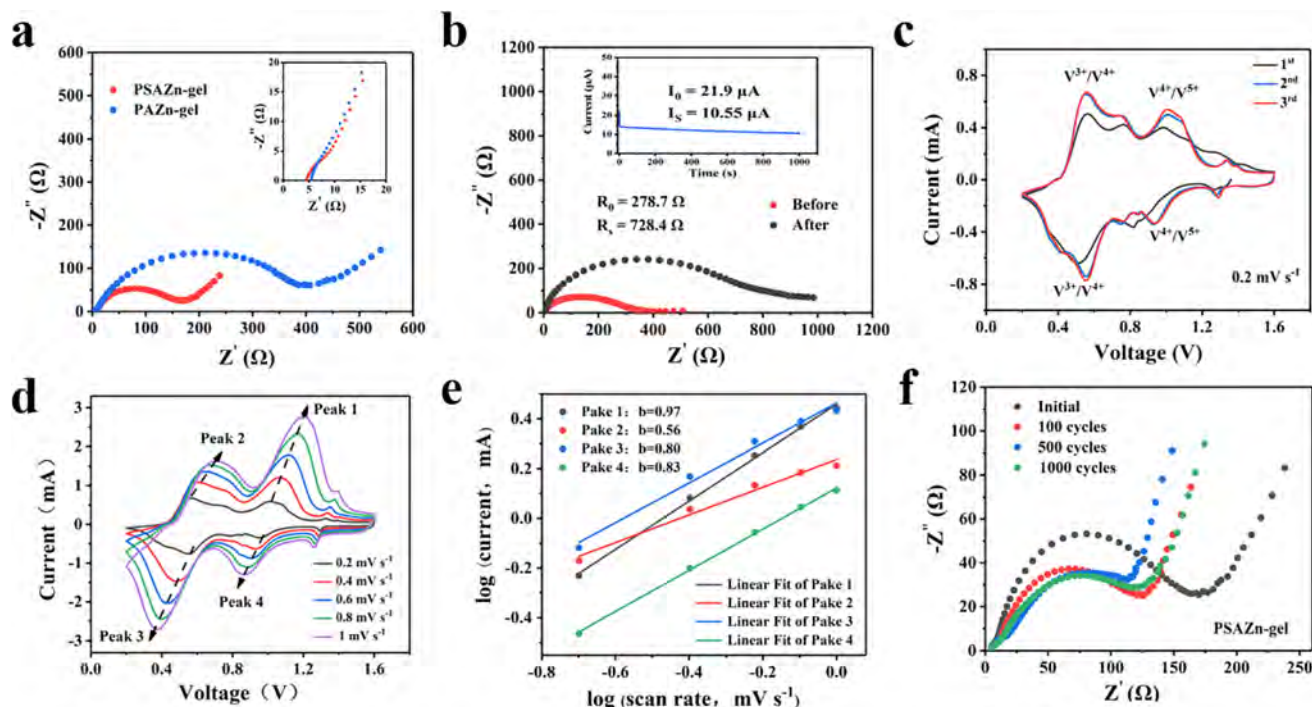


Fig. 2 Electrochemical performance of hydrogel electrolytes. (a) EIS plots of PSAZn-gel and PAZn-gel electrolytes in the frequency range of 0.01 Hz to 100 kHz (inset shows a zoomed-in view of the high-frequency region). (b) Characterization of the Zn²⁺ ion transference number of PSAZn-gel electrolyte (inset shows the corresponding *i*-*t* curve). (c) CV curves of PSAZn-gel electrolyte at a scan rate of 0.2 mV s⁻¹. (d) CV curves of PSAZn-gel electrolyte at different scan rates and (e) linear fits of log(current) versus log(scan rate) for the four peaks in the CV curves. (f) EIS changes of PSAZn-gel electrolyte before and after cycling.

form a stable hydration layer with H₂O, which further weakened the coordination between Zn²⁺ and H₂O, thus reducing the resistance during Zn²⁺ transport.⁴² Under the effect of these combined factors, the ion transport ability of Zn²⁺ in PSAZn-gel electrolyte is optimized.

The kinetic processes of redox reactions of NHVO cathode materials in ZIBs with different hydrogel electrolytes were investigated by cyclic voltammetry (CV). As shown in Fig. 2c, two distinct pairs of redox peaks can be observed in the CV curves. Among them, a pair of peaks located at 0.56/0.54 V indicates that redox reactions of V³⁺/V⁴⁺ occurred during Zn²⁺ insertion/extraction, and a pair of peaks located at 1.00/0.95 V indicates that redox reactions of V⁴⁺/V⁵⁺ occurred. In addition, except for the cyclic curve of the first loop, the curves of the 2nd–3rd loops almost overlapped and clear redox peaks can still be observed, which proves that NHVO has good reversibility during charge/discharge cycles. The CV curves of ZIBs composed of PSAZn-gel and PAZn-gel electrolytes were obtained separately at the same scan rate (Fig. S9†). The CV curves of the two electrolytes are similar, but the PSAZn-gel electrolyte based ZIB shows higher peak current and larger curve areas, indicating a higher utilization of the cathode active material in this system.⁴³ To further investigate the reaction kinetics of Zn²⁺ in the hydrogel electrolyte, the CV curves of Zn||PSAZn-gel||NHVO were obtained at different scan rates (Fig. 2d). The two pairs of distinct oxidation and reduction peaks in the curve were analyzed. The

relationship between the peak current and the scan rate can be expressed by using eqn (3):⁴⁴

$$i = av^b/\log(i) = b \log(v) + \log(a) \quad (3)$$

where *i* is the peak current, *v* is the scan rate, and *a* and *b* are variables. *b* = 0.5 and 1 indicate that the charge storage of the electrode material is controlled by diffusion and surface capacitance, respectively. As shown in Fig. 2e, a linear fit is performed by fitting the logarithm of the peak and sweep rates. The *b* values of the four peaks were calculated to be 0.97, 0.56, 0.80, and 0.83, respectively, indicating that the electrochemical behavior of the battery is controlled by both ion diffusion and capacitance.

To verify the stability of the electrode/electrolyte interface of the ZIBs during cycling, electrochemical impedance spectroscopy (EIS) analyses were performed on the battery in the initial state and after 100, 500, and 1000 cycles, respectively. As shown in Fig. 2f, the *R*_{ct} gradually decreases with the increase in the cycling number in the first 500 cycles. This is attributable to the fact that with the electrochemical reaction, the electrode active material is gradually wetted by the PSAZn-gel electrolyte, and the interfacial affinity between them is stronger. More importantly, the outstanding interfacial affinity properties can effectively inhibit the occurrence of Zn anode surface passivation and regulate the ion transport and deposition during the process of the electrochemical reaction, thus reducing the charge transfer resistance. The *R*_{ct} increases after 1000 cycles,

which may be due to some unavoidable Zn anode dendrites and interfacial side reactions that lead to an increase in interfacial resistance as the cycling number increases. However, it is still lower than the interface resistance measured in the initial state, which proves that the electrode–electrolyte interface is stable during the charging/discharging cycles. In contrast, the R_{ct} of the battery assembled with pure PAZn-gel electrolyte increases continuously with cycling as seen from Fig. S10,[†] which makes the battery decay significantly.

The Zn||electrolyte||NHVO cells were assembled using the two hydrogel electrolytes as shown in the assembly flow in Fig. S7.[†] As shown in Fig. 3a, the PSAZn-gel electrolyte battery has an initial discharge specific capacity of 300 mA h g⁻¹ at a current density of 0.5 A g⁻¹ and reaches a maximum discharge capacity of 355 mA h g⁻¹ after 8 charge and discharge cycles, with a capacity retention of 97.0% of the maximum capacity after 200 cycles. In contrast, the initial discharge capacity of the battery

with PAZn-gel electrolyte is only 257 mA h g⁻¹, and only 84.4% capacity is retained after 200 cycles. This demonstrates that the addition of SBMA not only improves the cycling stability of the battery but also substantially increases the utilization of the cathode active material. As shown in Fig. 3b and c, the rate performance of the cathode active material in different electrolytes was evaluated at different current densities from 0.5 to 5 A g⁻¹. The specific capacities of the PSAZn-gel electrolyte ZIBs reach 381, 366, 338, 319, 302, and 288 mA h g⁻¹ at current densities of 0.5, 1, 2, 3, 4, and 5 A g⁻¹, respectively, which are significantly higher than those of the PAZn-gel electrolyte based ZIBs. When a current of 0.5 A g⁻¹ was reapplied to the cell, the PSAZn-gel electrolyte ZIBs can still reach an initial discharge capacity of 378 mA h g⁻¹ with a high capacity retention of 99.2%, demonstrating excellent electrochemical reversibility. The capacity of the present work at different current densities was compared with that in other studies, showing a high

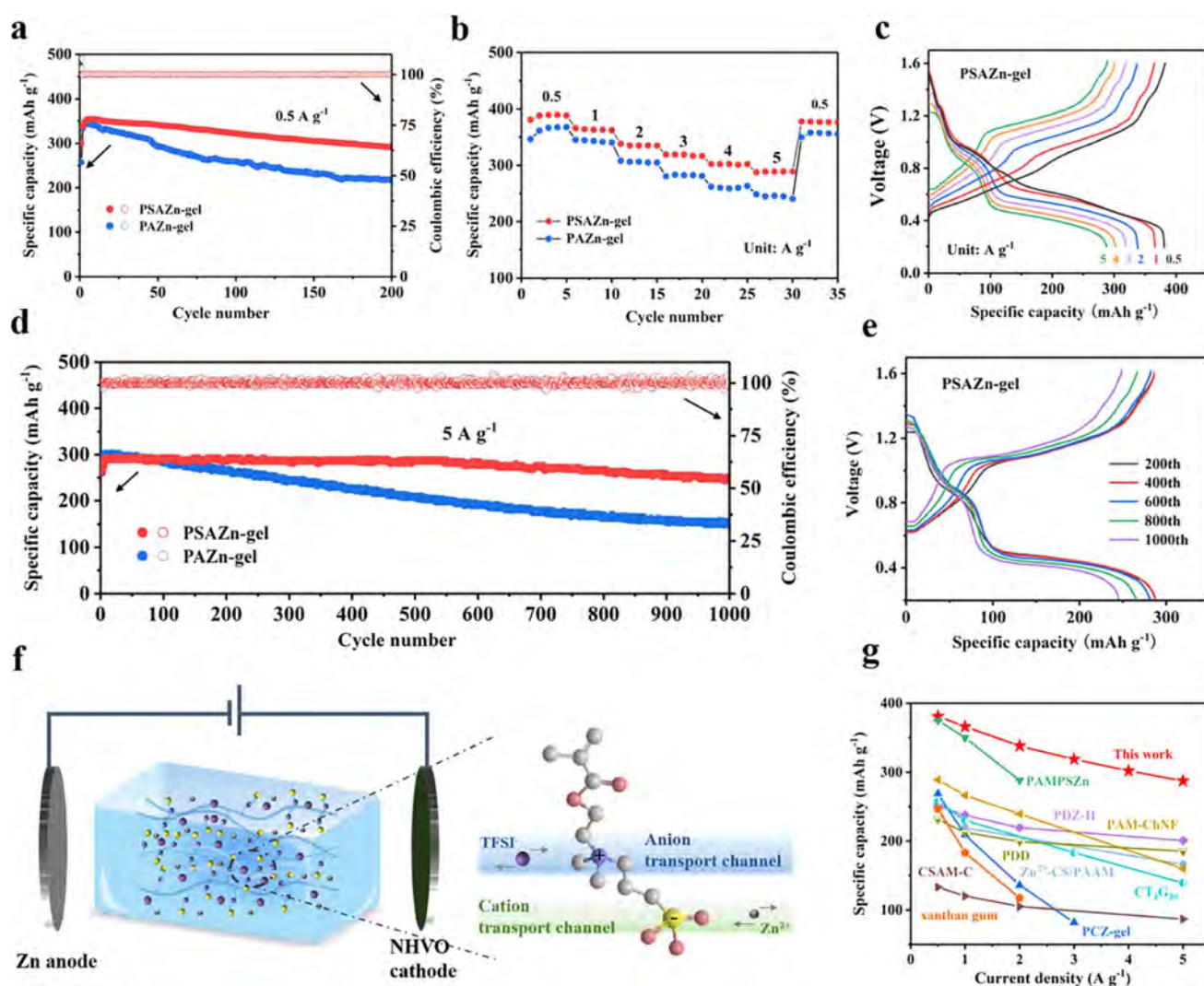


Fig. 3 Electrochemical performance of Zn||NHVO coin cells assembled with PSAZn-gel and PAZn-gel electrolytes. (a) Cycling performance at 0.5 A g⁻¹. (b) Cycling performance at different current rates and (c) charge–discharge curves. (d) Cycling performance at 5 A g⁻¹ and (e) corresponding charge/discharge curves at different cycle numbers. (f) Schematic diagram of ion migration channels of PSAZn-gel electrolyte. (g) Comparison plot of the specific capacity of the present work with the reported work at different current densities.^{14,37,43,45–50}

capacity advantage (Fig. 3g).^{14,37,43,45–50} Moreover, the stability of the battery was tested at a high current density of 5 A g^{-1} (Fig. 3d), and the battery has a surprisingly high specific capacity of 292 mA h g^{-1} . The specific capacity can still reach 249 mA h g^{-1} after 1000 cycles, with a capacity retention of 94.7%. The charge–discharge curves shown in Fig. 3e show that even after 1000 cycles, there is still an obvious voltage plateau, which corresponds to the two pairs of redox peaks in the CV curves in Fig. 2c, demonstrating the excellent cycling stability of ZIBs. In contrast, the electrochemical stability of ZIBs with PAZn-gel as the electrolyte is inferior (Fig. 3d and S11†). It is important to note that the battery capacity shows an increase during the first few cycles. This situation has also occurred in other studies, and may be due to electrochemical activation and gradual wetting of the active material by the electrolyte.^{51–53}

The PSAZn-gel electrolyte exhibits superior electrochemical performance mainly due to the special zwitterionic structure of SBMA which helps to promote the ordered migration of ions. The molecular chain of SBMA bears two charged groups, a negatively charged sulfonate group ($-\text{SO}_3^-$) and a positively charged quaternary ammonium group (R_4N^+), respectively. It has been shown in previous research studies that in polymer electrolytes, metal cations can migrate by jumping through constant complexation and de-complexation with polar groups (*e.g.*, $-\text{O}-$, $-\text{S}-$, $-\text{N}-$, *etc.*) on the polymer chain.^{54,55} In PSAZn-gel electrolyte, SBMA contains abundant polar groups and has negative binding energy with Zn^{2+} . Therefore, Zn^{2+} can complex and decomplex on the negatively charged $-\text{SO}_3^-$ sites on SBMA to realize jump migration, which constitutes a migration channel for Zn^{2+} on SBMA.³¹ Similarly, anions undergo jump migration at the R_4N^+ site, forming an anion migration channel on the SBMA chain. In this way, as shown in Fig. 3f, under the action of an external electric field, regularly arranged ion migration channels are formed along the positive and negative charged groups on both sides of the PSAZn-gel main chain, which promote the orderly high-speed migration of ions. On one hand, the dissolved Zn^{2+} ions and TFSI⁻ ions inside the electrolyte can easily overcome the electrostatic interactions between counterions and charged groups and thus can easily be separated. On the other hand, due to the electrostatic interaction between the charged groups and H_2O , a hydration layer is formed around the polymer chain, which further promotes the separation of Zn^{2+} ions and TFSI⁻ ions. Therefore, with the help of the special properties of the zwitterionic ions, the ions can migrate more easily inside the electrolyte in an orderly and fast manner, thus greatly enhancing the electrochemical performance of the battery.

To disclose the advantages of the hydrogel electrolyte more thoroughly, the cycled cell was disassembled to observe the surface morphology of the Zn anode. It is important to note that the gel adhering to the anode surface should be wiped off before observation. Due to the increased adhesion between the electrode/electrolyte after charging and discharging, the operation needs to be repeated several times to obtain a neat surface of Zn foil. Fig. 4a and b show the surface morphology of the anode of NHVO||PSAZn-gel||Zn cells after 300 and 500 charge/discharge cycles at a current density of 5 A g^{-1} , respectively. The SEM image clearly shows that even after 500 cycles, the surface of the

anode still maintains a regularly arranged laminar structure with no obvious dendrite formation. In contrast, NHVO||PAZn-gel||Zn cells show a haphazard arrangement of zinc on the anode surface after 300 cycles (Fig. 4c), and the surface is filled with zinc dendrites after 500 cycles (Fig. 4d). Even after 1000 cycles, few dendrites can be observed on the Zn anode surface of NHVO||PSAZn-gel||Zn cells (Fig. S12†).

The corrosion resistance of different electrolytes on the Zn anode was analyzed by using the Tafel curve. As shown in Fig. S13,† the corrosion potential of Zn in PSAZn-gel electrolyte is -0.050 V , which is higher than that of Zn in PAZn-gel electrolyte (-0.067 V). In addition, the corrosion current density of the Zn electrode in PSAZn-gel is lower, which proves that the corrosion protection of the Zn anode in PSAZn-gel electrolyte is more outstanding. In order to more clearly demonstrate the enhancing role of PSAZn-gel electrolyte in improving the stability of the anode, the Zn plating/stripping reversibility at the electrode/electrolyte interface was evaluated by assembling Zn||Zn symmetric cells at current densities of 1 mA cm^{-2} and 1 mA h cm^{-2} . The voltage–time curve shows that the Zn||PSAZn-gel||Zn cell can cycle steadily for 800 h and keep the voltage polarization stable, while the Zn||PAZn-gel||Zn cell shows increasing fluctuations in voltage after cycling for more than 300 h (Fig. S14†). It is obvious that the PSAZn-gel electrolyte has a great contribution to enhancing interfacial stability and inducing homogeneous zinc deposition. In addition, Zn||Cu asymmetric cells were assembled with two electrolytes to verify the cycling reversibility of Zn plating/stripping. As shown in Fig. S15a,† the Zn||Cu cell with PAZn-gel electrolyte shows rapid decline of coulombic efficiency after 20 cycles at 1 mA h cm^{-2} and 1 mA cm^{-2} . In contrast, the average coulombic efficiency of the Zn||Cu cell assembled with PSAZn-gel electrolyte remains above 99.0% after 150 cycles, demonstrating excellent reversible electrochemical stability. The detailed capacity–voltage curves demonstrated in Fig. S15b† also confirm the low voltage polarization and high reversibility. Similarly, the same results were demonstrated under 4 mA h cm^{-2} and 1 mA cm^{-2} conditions. From the results displayed in Fig. S15c and d,† it is evident that even under harsher conditions, Zn||PSAZn-gel||Cu still exhibits good voltage polarization and an impressive average coulombic efficiency of 98.8% after 600 cycles. These findings prove that PSAZn-gel can enhance the reversibility of Zn plating/stripping at the electrode/electrolyte interface, which is beneficial in suppressing the formation of zinc dendrites and promoting battery cycle stability.

Zn^{2+} exists as $[\text{Zn}(\text{H}_2\text{O})_6]^{2+}$ in aqueous solution, which severely hinders the deposition of Zn due to the strong interactions between Zn^{2+} and the surrounding H_2O molecules.⁴¹ Therefore, the effect of the solvated structure of Zn^{2+} ions on the Zn deposition/stripping process in the electrolyte is in-depth investigated by experimental and theoretical analyses. The desolvation process of $[\text{Zn}(\text{H}_2\text{O})_6]^{2+}$ in the PSAZn-gel electrolyte was analyzed based on density functional theory (DFT) calculations. As shown in Fig. 4e, the negative binding energy of Zn^{2+} with the sulfonate group on SBMA (-2.176 eV) is larger than that with the H_2O molecule (-0.862 eV), suggesting that Zn^{2+} prefers to bind with $-\text{SO}_3^-$. Similarly, the results of calculating

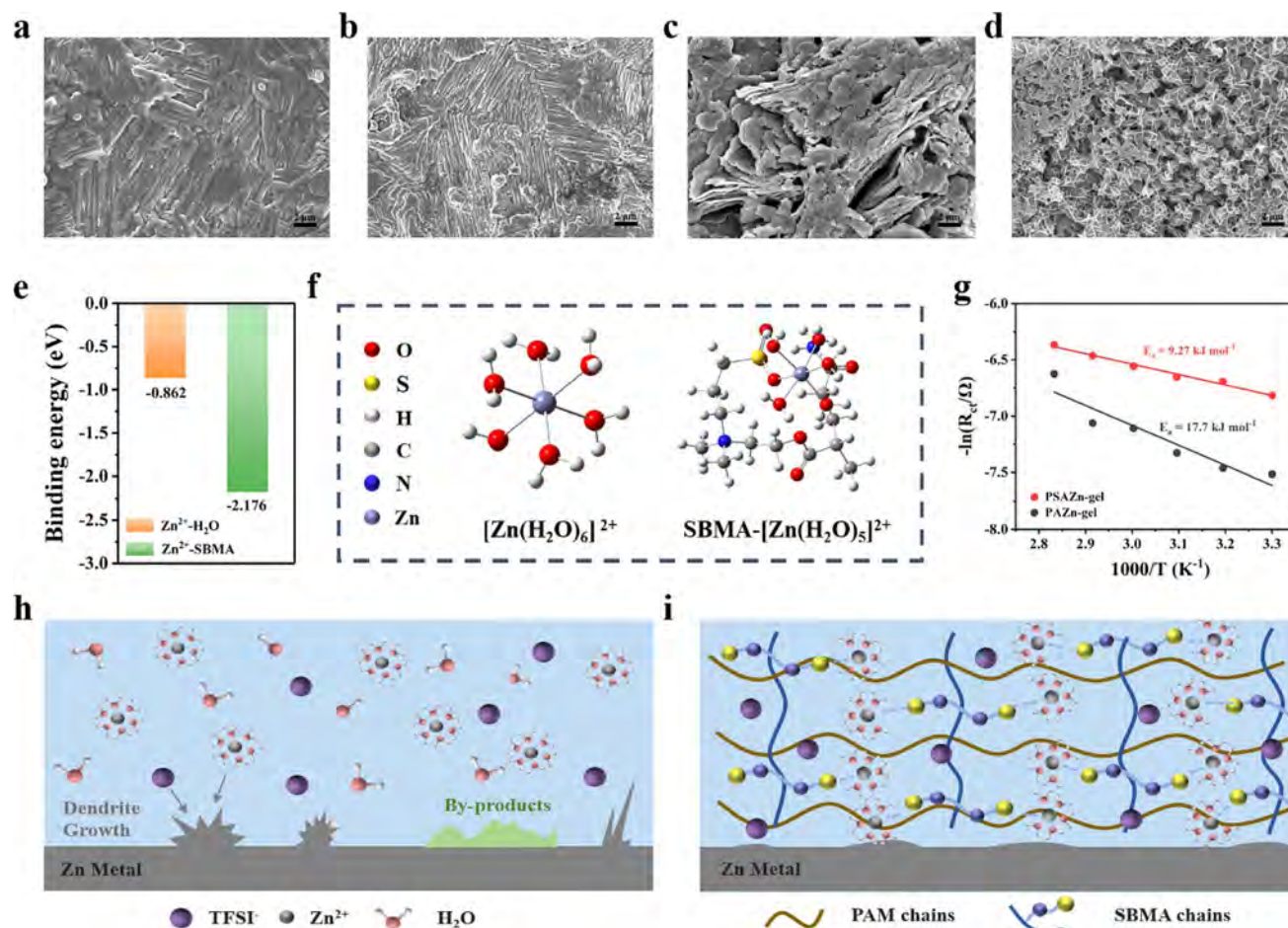


Fig. 4 Ion migration mechanism study in hydrogel electrolyte. (a) SEM images of the Zn anode surface after 300 and (b) 500 cycles of the NHVO||PSAZn-gel||Zn battery at 5 A g^{-1} . (c) SEM images of the Zn anode surface after 300 and (d) 500 cycles of the NHVO||PAZn-gel||Zn cell at 5 A g^{-1} . (e) Binding energy calculations for $\text{Zn}^{2+}\text{-H}_2\text{O}$ and $\text{Zn}^{2+}\text{-SBMA}$. (f) Simplified model for DFT calculations of $[\text{Zn}(\text{H}_2\text{O})_6]^{2+}$ and $\text{SBMA-}[\text{Zn}(\text{H}_2\text{O})_5]^{2+}$ in a solvated environment. (g) Arrhenius curves and the corresponding desolvation activation energies for two hydrogel electrolytes. (h) Reasons for the formation of dendrites on the surface of the Zn electrode and (i) the mechanism of inhibition of Zn dendrites by PSAZn-gel electrolyte.

the adsorption energies of H_2O and SBMA on the Zn(002) surface using first principles calculations support this idea. As shown in Fig. S16,[†] the adsorption energy of SBMA on the Zn surface is -1.92 eV , showing a more negative adsorption energy than that of the H_2O molecule (-0.28 eV). This proves that the sulfonate group on SBMA has a stronger affinity with the Zn surface, which is favorable for inducing the uniform deposition of Zn and thus inhibiting the growth of Zn dendrites. The desolvation ability of the electrolyte was further calculated by simplifying the solvation environment as shown in Fig. 4f and S17.[†] The results show that $\text{SBMA-}[\text{Zn}(\text{H}_2\text{O})_5]^{2+}$ (-21.64 eV) exhibits a higher desolvation energy than $[\text{Zn}(\text{H}_2\text{O})_6]^{2+}$ (-20.82 eV), which proves that the PSAZn-gel electrolyte can promote the desolvation of hydrated Zn^{2+} ions and reduce the energy loss, which in turn facilitates rapid and uniform Zn deposition. To provide additional evidence for the aforementioned calculation outcomes, the variable-temperature EIS curves of Zn||PSAZn-gel||Zn and Zn||PAZn-gel||Zn symmetric cells in the range of $30\text{--}80 \text{ }^\circ\text{C}$ were obtained. The activation energy (E_a) for

the desolvation of Zn^{2+} ions was calculated according to the Arrhenius eqn (4):^{56,57}

$$\frac{1}{R_{\text{ct}}} = A \exp\left(-\frac{E_a}{RT}\right) \quad (4)$$

where R_{ct} is the charge transfer resistance, A is the frequency factor, R is the gas constant, and T is the absolute temperature. As shown in Fig. S18 and S19,[†] Zn||PSAZn-gel||Zn exhibits more stable and smaller R_{ct} values at different temperatures. By fitting the linear relationship between R_{ct} and different test temperatures, the E_a values in different electrolytes were then obtained. As shown in Fig. 4g, the E_a of PSAZn-gel electrolyte is 9.27 kJ mol^{-1} , which is substantially smaller than that of PAZn-gel electrolyte (17.7 kJ mol^{-1}), proving that the PSAZn-gel electrolyte facilitates the desolvation and transportation of Zn^{2+} ions.

Combining the above experimental results and theoretical studies, the mechanism of Zn dendrite inhibition by the PSAZn-gel electrolyte was proposed. As shown in Fig. 4h, during the electrodeposition of Zn^{2+} ions tend to be deposited at higher

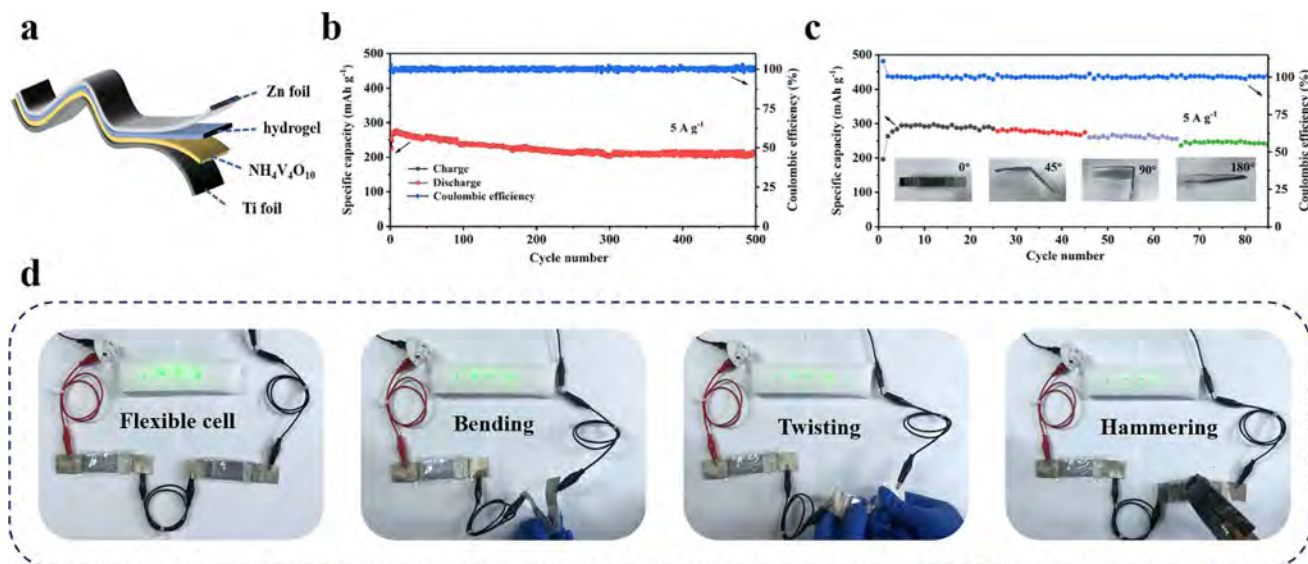


Fig. 5 Electrochemical performance and application of sandwich structure Zn||PSAZn-gel||NHVO cells. (a) Schematic diagram of the assembly. (b) Cycling performance at 5 A g^{-1} current density. (c) Cycling performance at different bending angle variations from 0° – 180° . (d) The LEDs are still illuminated when the battery is bent, twisted and hammered.

energy locations due to the inhomogeneous electric field distribution on the electrode surface, leading to rampant growth of Zn dendrites on the surface.⁵⁸ What's more, Zn^{2+} tends to form $[\text{Zn}(\text{H}_2\text{O})_6]^{2+}$ solvation shell layers with active H_2O molecules in the electrolyte. In a liquid environment, the weakening of the O–H bond by the strong interaction between Zn^{2+} and H_2O molecules makes the H_2O molecules in the solvation layer easily dissociate into H^+ and OH^- . H^+ accumulates on the Zn surface and reacts with it, generating H_2 , which leads to an increase in pH within the electrolyte and accelerates the surface-side reactions. A series of uncontrolled depositions lead to massive dendrite generation and irreversible exchange of Zn/ Zn^{2+} . As shown in Fig. 4i, the charged groups along the PSAZn-gel chains can form ion migration channels. Under an external electric field, Zn^{2+} cations and TFSI^- anions undergo directional movement, which reduces the migration energy barrier generated by electrostatic attraction and accelerates the rapid ion transport. In addition, the $-\text{SO}_3^-$ group on the PSAZn-gel chain tends to coordinate with Zn^{2+} , replacing a portion of the H_2O molecules in the solvated shell layer around Zn^{2+} to form a $[(\text{PSAZn-gel})-\text{Zn}(\text{H}_2\text{O})_5]^{2+}$ coordination structure. This accelerates the desolvation process of zinc ions, realizes the rapid and uniform deposition of Zn^{2+} , and effectively inhibits the formation of Zn dendrites.

2.3 Performance and application of the Zn||NHVO flexible battery

The PSAZn-gel electrolyte was sandwiched between the Zn foil and NHVO@Ti foil to prepare a sandwich structure of a solid-state flexible cell (Fig. 5a). As shown in Fig. 5b, the flexible ZIBs retain 96.9% capacity after 500 charge and discharge cycles at 5 A g^{-1} , and the average Coulomb efficiency can reach 100.0%. The flexible ZIBs were tested in extreme experiments such as bending, twisting and hammering. As shown in Fig. 5c, the

packaged sandwich structure battery was tested by bending cycles at different angles of 0° , 45° , 90° and 180° . Note that since the battery has a performance activation phase during the first few cycles of charging and discharging, the charge–discharge test was repeated for 25 cycles at 0° and 20 cycles for other bending angles. After 85 cycles, the battery still maintains an average coulombic efficiency close to 100.0%. The capacity retention rate and discharge specific capacity are shown in Fig. S20a and b.† Even though the capacity decreases after bending, the working process remains stable. As shown in Fig. S20c and d,† the capacity of the flexible ZIBs can still be maintained at 96.6% after 200 repetitions of twisting, with significant mechanical stability against external deformation. The battery was continuously hammered four more times, and as shown in Fig. S20e and f† the capacity retention rate was more than 97%, proving that the flexible ZIBs are able to withstand problems such as sudden impacts that may occur in real-world application situations. Furthermore, the battery can still power a string of LEDs under different types of external damage, such as bending, twisting and hammering (Fig. 5d), showing application prospects in harsh wearable application scenarios.

3. Conclusion

In summary, we have prepared a zwitterionic hydrogel electrolyte (PSAZn-gel electrolyte) for the fabrication of zinc-ion batteries (ZIBs) with excellent electrode/electrolyte interface stability and long cycle life. Charged groups on the zwitterionic polymer chains establish separated anion and cation migration channels that regulate ion transport. As a result, the PSAZn-gel electrolyte has an ionic conductivity of 59.0 mS cm^{-1} and a high Zn^{2+} transference number of 0.81. Moreover, the sulfonate group ($-\text{SO}_3^-$) on the SBMA chain promotes the desolvation

process of hydrated zinc ions and inhibits the generation of zinc dendrites and side reactions. The Zn||NH₄V₄O₁₀ battery prepared with PSAZn-gel electrolyte has excellent long-term cycle performance with 94.7% capacity retention after 1000 cycles at 5 A g⁻¹. The designed and prepared flexible planar structure battery also has excellent cycling performance, with a capacity retention of 96.9% after 500 cycles at 5 A g⁻¹. The LEDs can still work even under external damage, offering great potential for flexible wearable applications.

4. Experimental section

4.1 Materials

[2-(Methacryloyloxy)ethyl]dimethyl-(3-sulfopropyl) acrylamide (SBMA), acrylamide (AM), potassium peroxydisulfate (KPS), ammonium metavanadate (NH₄VO₃), β-cyclodextrin, oxalic acid (C₂H₂O₄) and *N,N'*-methylenebis(acrylamide) (Adamas, 99%, MBAA) were purchased from Greagent (Shanghai Titan Scientific Co., Ltd.). Zinc bis(trifluoromethyl sulfonyl)imide (Zn(TFSI)₂) was obtained from DADO New Material. Deionized (DI) water was used in all the experiments.

4.2 Preparation of PSAZn-gel electrolytes and PAZn-gel electrolytes

PSAZn-gel electrolytes and PAZn-gel electrolytes were prepared by the one-pot synthesis method. SBMA (1.5 g), AM (0.5 g), and Zn(TFSI)₂ (1 M) were dissolved in deionized water (5 mL), and then MBAA (0.5 wt%) and APS (1 wt%) were added and injected into glass molds after stirring and dissolving. Finally, the polymerized hydrogel electrolyte was obtained by thermally initiated curing at 60 °C for 5 h. The PAZn-gel electrolyte was prepared as a control using the same method without the addition of SBMA.

4.3 Preparation of the NH₄V₄O₁₀ (NHVO) cathode

Ammonium vanadate (NH₄V₄O₁₀) cathodic material was synthesized by the hydrothermal synthesis method (Fig. S6†). First, NH₄VO₃ (0.58 g) was dissolved in deionized water (70 mL), and a yellow solution was obtained by stirring. Then β-cyclodextrin (0.68 g) and anhydrous oxalic acid (H₂C₂O₄) (0.68 g) were added to the above yellow solution. The solution was transferred to a 100 mL Teflon-lined autoclave with stirring and the reaction was carried out at 120 °C for 10 h. After the reaction was completed, the samples were washed several times with deionized water and anhydrous ethanol, respectively. Finally, the samples were dried in a vacuum drying oven at 80 °C for 24 h to obtain NHVO powder.

The NHVO powder, conductive carbon black Super-P, and PVDF were ground and mixed at a mass ratio of 7 : 2 : 1, and then the obtained cathode slurry was evenly coated on the Ti foil and dried in a vacuum at 70 °C overnight to ensure that a thoroughly dried cathode sheet was obtained. The electrode sheets were punched into 10 mm diameter round cathode discs and cut into 1 cm × 3 cm rectangular electrode sheets for use.

4.4 Materials characterization

Fourier transform infrared (FTIR) spectra of the hydrogels were measured using an FTIR spectrometer (Nicolet iS5, Thermo Fisher, USA) in the wave number range of 500 to 4000 cm⁻¹. X-ray diffraction (XRD) analyses were performed on a D8 ADVANCE diffractometer for the cathode powder samples and the determination of the surface components of the zinc foil. The spectra were obtained using Cu Kα radiation ($\lambda = 1.5418 \text{ \AA}$) in the range of 5–80° in the 2θ region at 40 kV and 15 mA. The transmittance of PSAZn-gel hydrogels was determined using a UV-vis ultraviolet-visible spectrometer (PerkinElmer, USA) in the wavelength range of 400–800 nm. Scanning electron microscopy (SEM, SU8220, Hitachi, Japan) was used to observe the morphology of the network structure of the hydrogel cross-section and the surface of the zinc foil. Before the characterization of the hydrogels, the samples were all subjected to freeze-drying. Tensile tests were carried out using a universal tensile machine (CMT6103, MTS, USA) and a 1000 N load cell. Cyclic loading–unloading experiments (predetermined strain of 100%) and fracture tensile experiments were performed on hydrogels (30 × 17.5 × 1 mm) at a rate of 30 mm min⁻¹ respectively. Adhesion between hydrogels and different substrates was tested by bonding experiments. Hydrogels (diameter: 12 mm) laminated on a circular indenter were made to come in contact with the substrate on a flat plate by applying a pre-pressure of 20 N for 90 s, and then rapidly peeled off.

4.5 Electrochemical measurements

Electrochemical properties were tested using an electrochemical workstation (MAC90596, Multi Autolab M204, Switzerland), mainly including cyclic voltammetry (CV), electrochemical impedance spectroscopy (EIS), and linear scan voltammetry (LSV). The constant-current charge/discharge curves, long-cycle performance, and multiplier performance of the batteries at different current densities were tested using a battery test system (CT2001A, LAND, China).

Hydrogel with a thickness of 1 mm was cut into 14 mm diameter discs and used as the electrolyte and diaphragm part of the battery. The NHVO cathode sheet (10 mm) was used as the cathode and zinc foil (12 mm) was used as the anode to assemble CR2016 type coin cells for most of the battery electrochemical performance tests. Among them, CV tests were performed on NHVO||Zn cells with different gel systems in the voltage range of 0.2–1.6 V at a scanning speed of 0.2–1 mV s⁻¹. Similarly, Zn||Zn cells were assembled with Zn foil as the working electrode and counter electrode, respectively, and hydrogel as the electrolyte. Zn||Cu cells were assembled with Zn foil as the working electrode, Cu foil as the counter/reference electrode, and hydrogel as the electrolyte. The long-term cycle test of Zn plating/stripping was performed on a LAND. Additionally, the Zn²⁺ transference number of Zn||PSAZn-gel||Zn was tested by a combination of the chrono-current method (*i-t*) and electrochemical impedance method with a constant polarization potential set at 10 mV. In addition, the hydrogel was cut into discs of the same size as the stainless steel (SS) electrode diameter (15.8 mm) and placed between the two SS electrodes to

assemble CR2023 type coin cells. The corrosion Tafel curves were obtained using a Zn||Zn symmetric coin cell with the voltage range set to $-1-1$ V and a scan rate of 5 mV s^{-1} .

The hydrogel with a thickness of 1 mm was cut into a rectangle of $1.5 \text{ cm} \times 3.5 \text{ cm}$, the coating area of the positive material on the titanium foil was $1 \text{ cm} \times 3 \text{ cm}$, and the sandwich structure battery was assembled as shown in Fig. 5a. Finally, it was vacuum sealed with a plastic sealing film to maintain better contact at the cell interface as well as for long-term stable use. The sandwich battery is tested for long-term cycle stability and changes in charge and discharge performance at different angles of bending.

4.6 Calculation

In order to find the optimal adsorption structures of water with PSAZn-gel, *ab initio* molecular dynamic simulations for a total time of 5 ps were then performed with the GFN-force-field (GFN-FF) method using the xTB program,⁵⁹ and the trajectory was saved every 1 fs. After the molecular dynamic simulation, one hundred complex structures with the lowest energy were extracted from the trajectory data and then optimized with the GFN2-xTB method. After the preliminary structural optimization, the cluster with the lowest energy was selected as the optimal structure. These structures were then optimized under the framework of density functional theory (DFT) at PBE0-D3/def2-SVP.^{60,61} The SMD (solvation model based on density)⁶² implicit solvent model was used to describe the solvation effect of water. The binding energy of the complex was calculated using eqn (5):

$$E(\text{binding}) = E(A + B) - E(A) - E(B) \quad (5)$$

where $E(A)$ and $E(B)$ are the energy of isolated molecules, $E(A + B)$ is the total energy of the complex structure.

First principles calculations are performed to reveal the mechanism by using the Vienna *ab initio* simulation package.^{63,64} The program has the projected enhancement wave pseudopotential⁶⁵ and the generalized gradient approximation of Perdew, Burke and Ernzerhof (PBE) exchange correlation functional,⁶⁶ which are used to optimize the structure and obtain the free energy of all structures. The cutoff energy of the plane wave basis set is 400 eV and a Monkhorst–Pack mesh of $3 \times 3 \times 1$ is used in K-sampling in the adsorption energy calculation. The electronic self-consistent iteration is set to 10^{-5} eV, and the positions of all of the atoms are fully relaxed until the residual force on each atom is below 0.03 eV \AA^{-1} . A 15 \AA vacuum layer along the z-direction is applied to avoid periodic interactions.

The complex structures of $\text{PSAZn}[\text{Zn}(\text{H}_2\text{O})_5]^{2+}$ and $[\text{Zn}(\text{H}_2\text{O})_6]^{2+}$ were also calculated using the same method. The vibrational frequency analysis was carried out for these optimized structures to obtain the zero-point energy and free energy corrections. The thermodynamic correction terms and Gibbs free energy of these structures at 298.15 K were then obtained using the Shermo program.⁶⁷ The desolvation energy was calculated using eqn (6):

$$\Delta G = G\left([\text{PSAZn}]_m[\text{Zn}(\text{H}_2\text{O})_n]^{2+}, \text{sol}\right) - G(\text{Zn}^{2+}, \text{gas}) - nG(\text{H}_2\text{O}, \text{sol}) - mG(\text{PSAZn}) \quad (6)$$

The GaussView package⁶⁸ was used to plot the color-filled iso-surface graphs to visualize the molecular electrostatic potential (MESP).

Conflicts of interest

The authors declare no conflict of financial interest.

Acknowledgements

This work was financially supported by the National Natural Science Foundation of China (Grant No. 62122080 62261136551), Natural Science Foundation of Shanghai (22ZR1481700 and 22dz1205000), and the Priority Academic Program Development of Jiangsu Higher Education Institutions (PAPD).

References

- W. X. Liu, X. X. Niu, J. X. Feng, R. L. Yin, S. L. Ma, W. B. Que, J. L. Dai, J. W. Tang, F. F. Wu, W. H. Shi, X. J. Liu and X. H. Cao, *ACS Appl. Mater. Interfaces*, 2023, **15**, 15344–15352.
- W. J. Liu, W. X. Liu, T. Hou, J. Y. Ding, Z. G. Wang, R. L. Yin, X. Y. San, L. G. Feng, J. Luo and X. J. Liu, *Nano Res.*, 2024, **17**(6), 4797–4806.
- J. Yu, Z. Li, C. Wang, X. M. Xu, T. Liu, D. F. Chen, Z. P. Shao and M. Ni, *J. Colloid Interface Sci.*, 2024, **661**, 629–661.
- F. Mo, G. Liang, Z. Huang, H. Li, D. Wang and C. Zhi, *Adv. Mater.*, 2020, **32**, e1902151.
- P. Yang, J. L. Yang, K. Liu and H. J. Fan, *ACS Nano*, 2022, **16**, 15528–15536.
- J. Wang, S. Li, F. Yi, Y. Zi, J. Lin, X. Wang, Y. Xu and Z. L. Wang, *Nat. Commun.*, 2016, **7**, 12744.
- L. Hong, L. Y. Wang, Y. Wang, X. Wu, W. Huang, Y. Zhou, K. X. Wang and J. S. Chen, *Adv. Sci.*, 2022, **9**, 2104866.
- C. Xu, B. Li, H. Du and F. Kang, *Angew. Chem.*, 2012, **124**, 957–959.
- L. Hong, X. Wu, Y. S. Liu, C. Yu, Y. Liu, K. Sun, C. Shen, W. Huang, Y. Zhou and J. S. Chen, *Adv. Funct. Mater.*, 2023, 2300952.
- Y. Wang, Z. Wang, F. Yang, S. Liu, S. Zhang, J. Mao and Z. Guo, *Small*, 2022, **18**, 2107033.
- P. Lin, J. Cong, J. Li, M. Zhang, P. Lai, J. Zeng, Y. Yang and J. Zhao, *Energy Storage Mater.*, 2022, **49**, 172–180.
- M. Sun, G. Ji and J. Zheng, *Chem. Eng. J.*, 2023, **463**, 142535.
- R. Qi, W. Tang, Y. Shi, K. Teng, Y. Deng, L. Zhang, J. Zhang and R. Liu, *Adv. Funct. Mater.*, 2023, 2306052.
- S. Huang, L. Hou, T. Li, Y. Jiao and P. Wu, *Adv. Mater.*, 2022, **34**, 2110140.
- F. Mo, M. Cui, N. He, L. Chen, J. Fei, Z. Ma, S. Yu, J. Wei and Y. Huang, *Mater. Res. Lett.*, 2022, **10**, 501–520.
- H. Li, Z. Liu, G. Liang, Y. Huang, Y. Huang, M. Zhu, Z. Pei, Q. Xue, Z. Tang and Y. Wang, *ACS Nano*, 2018, **12**, 3140–3148.

- 17 S. Huang, F. Wan, S. Bi, J. Zhu, Z. Niu and J. Chen, *Angew Chem., Int. Ed.*, 2019, **58**, 4313–4317.
- 18 G. Cao, L. Zhao, X. Ji, Y. Peng, M. Yu, X. Wang, X. Li and F. Ran, *Small*, 2023, 2207610.
- 19 T. N. T. Tran, D. Aasen, D. Zhalmuratova, M. Labbe, H. J. Chung and D. G. Ivey, *Batteries Supercaps*, 2020, **3**, 917–927.
- 20 C. Yan, Y. Wang, Z. Chen and X. Deng, *Batteries Supercaps*, 2021, **4**, 1627–1635.
- 21 H. Li, C. Han, Y. Huang, Y. Huang, M. Zhu, Z. Pei, Q. Xue, Z. Wang, Z. Liu and Z. J. Tang, *Energy Environ. Sci.*, 2018, **11**, 941–951.
- 22 D. Wang, H. Li, Z. Liu, Z. Tang, G. Liang, F. Mo, Q. Yang, L. Ma and C. J. Zhi, *Small*, 2018, **14**, 1803978.
- 23 S. M. Zhuo, M. Tang, Y. C. Wu, Y. Chen, S. L. Zhu, Q. Wang, C. Xia and C. L. Wang, *Nanoscale Horiz.*, 2019, **4**, 1092–1098.
- 24 F. Makhlooghiazad, L. A. O'Dell, L. Porcarelli, C. Forsyth, N. Quazi, M. Asadi, O. Hutt, D. Mecerreyes, M. Forsyth and J. M. Pringle, *Nat. Mater.*, 2022, **21**, 228–236.
- 25 R. Chen, Q. Liu, L. Xu, X. Zuo, F. Liu, J. Zhang, X. Zhou and L. J. Mai, *ACS Energy Lett.*, 2022, **7**, 1719–1727.
- 26 K. Leng, G. Li, J. Guo, X. Zhang, A. Wang, X. Liu and J. J. Luo, *Adv. Funct. Mater.*, 2020, **30**, 2001317.
- 27 Q. Fu, S. Hao, L. Meng, F. Xu and J. J. Yang, *ACS Nano*, 2021, **15**, 18469–18482.
- 28 H. J. Min, M. S. Park, M. Kang and J. H. Kim, *Chem. Eng. J.*, 2021, **412**, 127500.
- 29 C. Liu, F. Li, G. Li, P. Li, A. Hu, Z. Cui, Z. Cong and J. Niu, *ACS Appl. Mater.*, 2022, **14**, 9608–9617.
- 30 Q. He, G. Fang, Z. Chang, Y. Zhang, S. Zhou, M. Zhou, S. Chai, Y. Zhong, G. Cao and S. Liang, *Nano-Micro Lett.*, 2022, **14**, 93.
- 31 T. Wu, C. Ji, H. Mi, F. Guo, G. Guo, B. Zhang and M. Wu, *J. Mater. Chem. A*, 2022, **10**, 25701–25713.
- 32 H. Cha, J. Kim, Y. Lee, J. Cho and M. J. Park, *Small*, 2018, **14**, 1702989.
- 33 W. Diao, L. Wu, X. Ma, Z. Zhuang, S. Li, X. Bu and Y. Fang, *J. Appl. Polym. Sci.*, 2019, **136**, 47783.
- 34 Y. Ye, Y. Zhang, Y. Chen, X. Han and F. Jiang, *Adv. Funct. Mater.*, 2020, **30**, 2003430.
- 35 Y. Dai, Y. Zhang, P. Zhang, Y. Liu, S. Liu, J. Wang, W. Wu and J. Wang, *J. Power Sources*, 2024, **591**, 233891.
- 36 X. Peng, H. Liu, Q. Yin, J. Wu, P. Chen, G. Zhang, G. Liu, C. Wu and Y. Xie, *Nat. Commun.*, 2016, **7**, 11782.
- 37 J. Cong, X. Shen, Z. Wen, X. Wang, L. Peng, J. Zeng and J. Zhao, *Energy Storage Mater.*, 2021, **35**, 586–594.
- 38 L. Suo, Y.-S. Hu, H. Li, M. Armand and L. Chen, *Nat. Commun.*, 2013, **4**, 1481.
- 39 C. Y. Fu, Y. P. Wang, C. G. Lu, S. Zhou, Q. He, Y. Z. Hu, M. Y. Feng, Y. L. Wan, J. D. Lin, Y. F. Zhang and A. Q. Pan, *Energy Storage Mater.*, 2022, **51**, 588–598.
- 40 C. Tiypiboonchaiya, J. M. Pringle, J. Sun, N. Byrne, P. C. Howlett, D. R. MacFarlane and M. J. Forsyth, *Nat. Mater.*, 2004, **3**, 29–32.
- 41 W. Zhang, F. Guo, H. Mi, Z. S. Wu, C. Ji, C. Yang and J. Qiu, *Adv. Energy Mater.*, 2022, **12**, 2202219.
- 42 H. R. Wang, W. Wei, X. X. Liu, S. C. Xu, Y. F. Dong and R. H. He, *Energy Storage Mater.*, 2023, **55**, 597–605.
- 43 H. Zhang, X. Gan, Z. Song and J. Zhou, *Angew Chem., Int. Ed.*, 2023, **135**, e202217833.
- 44 D. Feng, Y. Jiao and P. Wu, *Angew Chem., Int. Ed.*, 2022, **135**, e202215060.
- 45 Y. Q. Liu, A. M. Gao, J. N. Hao, X. L. Li, J. Z. Ling, F. Y. Yi, Q. Z. Li and D. Shu, *Chem. Eng. J.*, 2023, **452**, 139605.
- 46 H. Lu, J. Hu, L. Wang, J. Li, X. Ma, Z. Zhu, H. Li, Y. Zhao, Y. Li and J. Zhao, *Adv. Funct. Mater.*, 2022, **32**, 2112540.
- 47 C. Liu, W. Xu, C. Mei, M. Li, W. Chen, S. Hong, W. Y. Kim, S. y. Lee and Q. Wu, *Adv. Energy Mater.*, 2021, **11**, 2003902.
- 48 M. Chen, J. Chen, W. Zhou, X. Han, Y. Yao and C. P. Wong, *Adv. Mater.*, 2021, **33**, 2007559.
- 49 M. Peng, X. Tang, K. Xiao, T. Hu, K. Yuan and Y. Chen, *Angew. Chem., Int. Ed.*, 2023, e202302701.
- 50 Y. Chen, J. Zhao and Y. Wang, *ACS Appl. Energy Mater.*, 2020, **3**, 9058–9065.
- 51 X. Li, M. Li, Q. Yang, H. Li, H. Xu, Z. Chai, K. Chen, Z. Liu, Z. Tang, L. Ma, Z. Huang, B. Dong, X. Yin, Q. Huang and C. Zhi, *ACS Nano*, 2020, **14**, 541–551.
- 52 D. Sha, C. Lu, W. He, J. Ding, H. Zhang, Z. Bao, X. Cao, J. Fan, Y. Dou, L. Pan and Z. Sun, *ACS Nano*, 2022, **16**, 2711–2720.
- 53 X. Zhu, Z. Cao, W. Wang, H. Li, J. Dong, S. Gao, D. Xu, L. Li, J. Shen and M. Ye, *ACS Nano*, 2021, **15**, 2971–2983.
- 54 J. B. Yang, Z. Xu, J. J. Wang, L. G. Gai, X. X. Ji, H. H. Jiang and L. B. Liu, *Adv. Funct. Mater.*, 2021, **31**, 2009438.
- 55 W. S. Young, W. F. Kuan and T. H. Epps, *J. Polym. Sci., Part B: Polym. Phys.*, 2014, **52**, 1–16.
- 56 Y. Yang, C. Liu, Z. Lv, H. Yang, Y. Zhang, M. Ye, L. Chen, J. Zhao and C. C. Li, *Adv. Mater.*, 2021, **33**, 2007388.
- 57 X. Qi, F. Xie, Y.-T. Xu, H. Xu, C.-L. Sun, S.-H. Wang, J.-Y. Hu and X.-F. Wang, *Chem. Eng. J.*, 2023, **453**, 139963.
- 58 X. Li, D. Wang and F. Ran, *Energy Storage Mater.*, 2023, **56**, 351–393.
- 59 C. Bannwarth, E. Caldeweyher, S. Ehlert, A. Hansen, P. Pracht, J. Seibert, S. Spicher and S. Grimme, *Wiley Interdiscip. Rev.: Comput. Mol. Sci.*, 2021, **11**, e1493.
- 60 a. Petersson, A. Bennett, T. G. Tensfeldt, M. A. Al-Laham, W. A. Shirley and J. Mantzaris, *J. Chem. Phys.*, 1988, **89**, 2193–2218.
- 61 G. Petersson and M. A. Al-Laham, *J. Chem. Phys.*, 1991, **94**, 6081–6090.
- 62 A. V. Marenich, C. J. Cramer and D. G. Truhlar, *J. Phys. Chem. B*, 2009, **113**, 6378–6396.
- 63 G. Kresse and J. Furthmuller, *Comput. Mater. Sci.*, 1996, **6**, 15–50.
- 64 M. D. Segall, P. J. D. Lindan, M. J. Probert, C. J. Pickard, P. J. Hasnip, S. J. Clark and M. C. Payne, *J. Phys.: Condens. Matter*, 2002, **14**, 2717–2744.
- 65 P. E. Blöchl, *Phys. Rev. B: Condens. Matter Mater. Phys.*, 1994, **50**, 17953–17979.
- 66 J. P. Perdew, K. Burke and M. Ernzerhof, *Phys. Rev. Lett.*, 1996, **77**, 3865–3868.
- 67 T. Lu and Q. Chen, *Comput. Theor. Chem.*, 2021, **1200**, 113249.
- 68 T. K. R. I. Dennington and J. Millam, *Semichem. Inc*, Shawnee Mission, KS, 2008.